A Computational Approach in Understanding the Low-Velocity Impact Behavior and Damage of 3D-Printed Polymer Lattice Structures

Abdalsalam Fadeel, Hasanain Abdulhadi, Raghavan Srinivasan, and Ahsan Mian

The remarkable mechanical characteristics of sandwich lattice structures have attracted the attention of many researchers and make it a good candidate for various applications. However, there is limited published research concerning the development of general-purpose dynamic models mimicking the impact behavior of lattice configurations made from polymeric materials. As such, the main focus of this research is to develop efficient computational finite element models simulating the dynamic impact behavior of various lattice configurations embedded in sandwich panels that are made from Acrylonitrile Butadiene Styrene (ABS) material. In this case, the sandwich panel consists of a 3D-printed polymer lattice core covered with the skin of a Kevlar sheet. Four designs with different configurations of lattice structures were investigated experimentally in previous studies. The first configuration was the basic body centered cubic (BCC) with unit cell dimensions of 5 mm × 5 mm × 5 mm, and a strut diameter of 1 mm. The second configuration was produced by adding the vertical struts at alternative nodes layer by layer, referred to as BCCA. The third configuration was created by adding the struts with uniform gradient distributions, termed as BCCG. The last configuration was designed by adding vertical struts at all nodes on the BCC configuration, denoted as BCCV. In this research, the FEA software ABAQUS Explicit was used to model all four configurations under low-velocity impact loads. Then, the results from the FEA modeling of the four different sandwich structures were compared with the experimental observations. Significantly, the good agreement in the results between the FEA and the experimental work reveals the capability of the developed models to capture the dynamic impact behavior of various lattice configurations and is considered the main contribution of the current research. In addition, in situ deformation along with failure mechanisms, detailed information, visualization, and sufficient data of the lattice impact test has been obtained through the developed models. This in turn leads to saving human time and effort, providing better realization and deep analysis of impact deformation behavior reducing the size of the experimental work and the expenses associated with it.

1. Introduction

Many studies have been conducted on the engineering sandwich lattice structure due to its promising behavior, such as improved flexural stiffness and energy absorption, as well as its lightweight properties (Ref 1-5). For these reasons, sandwich lattice structures have been adopted for many applications, as seen in the automobile, aerospace industry, and biomedical engineering. More specific applications of lattice structures include vehicle wing structures, gas turbine blades, tissue structures, and rib implants (Ref 6-9). In addition, the recent studies showed that the lattice generations made of biocompatible material could provide good environment for cell growth similar to what was provided by 3D-bioprinting technology used to create organoids (Ref 10). As future applications, the sandwich lattice structures could be combined with advanced materials or sensors such as flexible dielectric composite materials (Ref 11), glucose biosensor (Ref 12), chemoreceptive sensors (Ref 13), and biopolymeric adsorbent (Ref 14) in order to expand the range of lattice applications and enable the lattice structures to be used in energy storage applications, nonenzymatic sensing applications, detection of liquid petroleum gas, and fluoride removal from the drinking water. Due to the far-famed ability of honeycomb material to absorb energy, many investigations have been conducted on it in the recent decades (Ref 15-19). Recently, there is an increasing demand on the engineering applications that require higher energy absorption capabilities and shock absorbers, especially in the field of crashworthiness (Ref 20, 21). This in turn sheds light on the cellular materials, which are considered appropriate cores in the structural designs for a new era of sandwich structures. The mechanical properties of cellular materials can be adjusted by changing their topological design to enhance the capabilities of energy absorption and strength,

Abdalsalam Fadeel, Hasanain Abdulhadi, Raghavan Srinivasan, and **Ahsan Mian**, Department of Mechanical and Material Engineering, Wright State University, 3640 Colonel Glenn Hwy, Dayton, OH 45435. Contact e-mail: ahsan.mian@wright.edu.

along with keeping the weight light. For instance, metallic lattice structures developed at Liverpool have shown competitive mechanical properties such as stiffness and strength with the aluminum foam (Ref 22). Furthermore, it can offer many benefits such as thermal resistance, durability, low density, and lower cost (Ref 23). Up to this point, despite the fact that many researchers have performed studies in the area of sandwich structures, there is still lack of impact behavior information of polymeric lattice material and the associated FEA.

According to finite element methods (FEMs), it is difficult to simulate the general dynamic behaviors of lattice models when compared with static ones (Ref 18, 24). It has been found that the finite element simulation based on ABAQUS is capable of providing good approximation to the real experimental work (Ref 25). In this regard, the cellular material can be considered as homogeneous orthotropic material for simplification purposes when conducting FEA (Ref 23). At earlier studies, it was modeled based on Euler–Bernoulli beam elements using programming techniques, but recently the commercial finite element software ABAQUS has been frequently used to perform an efficient modeling (Ref 23). Identifying the proper element type and size will significantly help to achieve high accuracy and reduce the computational time (Ref 20, 21). To get better results, seeking for a good agreement with the experimental ones, the finite element mesh should be practical (Ref 26). This means that the mesh size should not be necessarily very fine since the associated computational cost or the simulation time will be very high. Similarly, adopting mesh with large element size leads to inaccurate results in most cases. Hence, the optimum finite element mesh should be identified carefully based on convergence analyses to obtain accurate results at least computational cost (Ref 26).

It is also worth mentioning that the models might be difficult to be generated via ABAQUS due to the complexity of many geometrical features. Consequently, it was recommended to be designed by SolidWorks 2017-version11. To achieve that, the models can be exported to ABAQUS via SolidWorks Associative Interface (Ref 27). This tool allows to transfer the parts or assemblies from SolidWorks to ABAQUS/CAE easily without losing any information (Ref 27). Also, it is easy to change any dimension or design in SolidWorks, and subsequently the ABAQUS model, without affecting any analytical features such as partitions, boundary conditions, data sets, and surfaces (Ref 27). For this reason, SolidWorks 2017-version11 with MMGS unit system (millimeters, gram, seconds) was used in the current manuscript. The structural parameters were the lattice geometries, for instance, strut diameter, strut length, unit cell size, and number of unit cells. However, it might require regenerating the mesh for the model with the same conditions applied through ABAQUS. For example, if any specific element size and number of elements are chosen, they are not automatically updated when modifying the geometry in Solid-Works or upgrading the model in ABAQUS. Moreover, it is necessary to preserve the units of the model for the consistency and keep them the same for both SolidWorks and ABAQUS models. In other words, if millimeters (mm) are used for the displacement units, and Mega Pascals (MPa) for the stress units, the mass has to be Tons (1000 kg) units instead of kilograms (kgs). Subsequently, the density will be plugged as Tons/mm^3 instead of kg/m^3.

The present work is based on the previous experimental investigations of sandwich structures fabricated with four different configurations of lattice cores (Ref 1). In this case,

FEM is used to model sandwich structures fabricated with ABS lattice cores under low-velocity impact loads and is compared with the experimental findings. Once validated, the FEA results are then used to reveal how the lattice geometrical shapes or strut distributions can influence the fracture damage in different layers in situ. In addition, the current study can be used to predict the impact behaviors of sandwich structures made from different lattice-strut diameters and various lattice-cell dimensions, thereby reducing the size and the cost of the experimental work as well as saving human time and effort.

2. Materials and Sample Design

In this research, four configurations of the sandwich structures under low-velocity impact have been investigated numerically. This sandwich structure is basically a lattice core made from ABS and covered with skin from a 0.89-mm-thick Kevlar 49 sheet. The first configuration is BCC with unit cell dimensions of 5 mm × 5 mm × 5 mm as shown in Fig. 1. The design simplicity and the printing capability of BCC configuration make it the first in the typical lattice chain. In other words, the BCC lattice is not complicated such that the integrity of the printed parts is guaranteed in most cases. The cells were arranged as 10 cells in X and Y directions with 4 levels in the Z direction. Eventually, the overall lattice dimensions of the core will be 50 mm × 50 mm × 20 mm. This cell arrangement was selected in order to validate the developed finite element models by comparing the results with the existing experimental work from the literature. In addition, it has been observed that the effect of boundaries on the equivalent lattice properties will be negligible if the lattice configurations have more than 3 cells in thickness direction (Ref 28). Besides, it can be observed from Fig. 1 that the cell layers in thickness direction are designated into four layers (I, II, III, and IV).

The other configurations were made by modifying BCC by adding vertical struts at the nodes located in different positions of the lattice by keeping the same patterns and layer arrangements. In this regard, BCCA (BCC with alternate vertical struts) was made by adding vertical strands in an alternative BCC cells as it can be seen in Fig. 1. This means that the vertical strands are added between the central nodes of the two layers I and II, and III and IV. For BCCG (BCC with gradient arrangements of vertical struts) configuration, the vertical bars were distributed gradually with a uniform arrangement as explained in Fig. 1. In this case, the vertical struts are distributed linearly in the thickness direction starting with the 32 to 111 struts in the downward thickness direction. This design is intended to have controlled progressive failure from the weakest layer (the least number of vertical struts) to the strongest layer (the most number of vertical struts). More details about BCCG configuration were explained in reference (Ref 1). BCCV (BCC with vertical struts) configuration was created by adding vertical struts at each node and layer through the whole lattice structure as shown in Fig. 1. In other words, BCCV includes two sets of the vertical struts. The first set connects the central nodes of all layers together, starting from the center of layer IV moving down till the center of layer I. The second set connects the outer nodes or the nodes located at the cell edges together, extending vertically from the top to the bottom of the entire lattice structure.
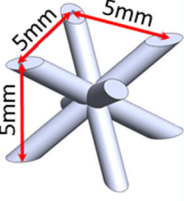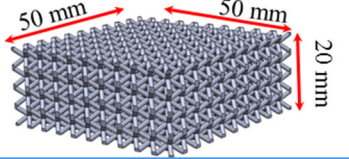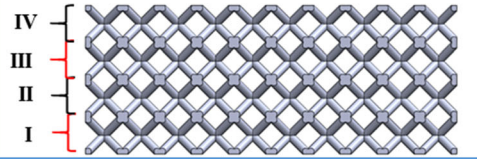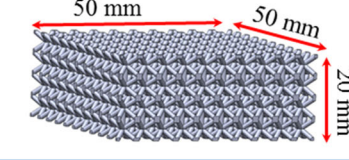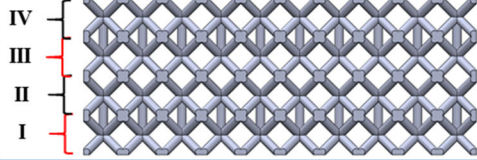
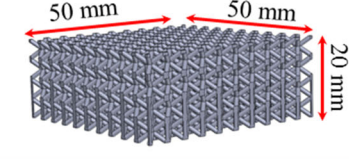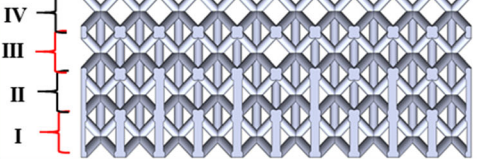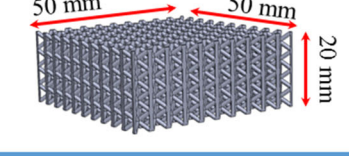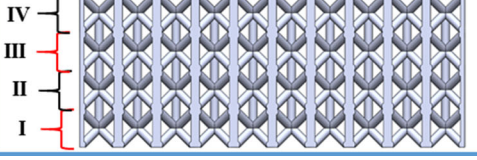| One-unit Cell	Configuration remarks	Configuration 3D view	Configuration side view
	BCC Regular pattern of BCC unit cells	50 mm, 50 mm, 20 mm	IV III II I
	BCCA BCC combined with alternative vertical struts between Layers I and II, and III and IV	50 mm, 50 mm, 20 mm	IV III II I
	BCCG BCC combined with vertical struts distributed with gradient arrangement, see ref. [1].	50 mm, 50 mm, 20 mm	IV III II I
	BCCV BCC combined with vertical struts at all nodes.	50 mm, 50 mm, 20 mm	IV III II I

Fig. 1 The lattice configuration designations

3. Results

3.1 Finite Element Modeling

ABAQUS 6.16 Explicit CAE 2016 finite element software was used to computationally analyze the sandwich structures. As mentioned before, the models were first designed in SolidWorks and were exported to ABAQUS/CAE via the tool of SolidWorks Associative Interface. This tool provides immediate connection between ABAQUS/CAE and the Solid-Works as shown in Fig. 2. By this means, the dimensions and the geometrical design can be easily changed through Solid-Works and, consequently, the model will be upgraded in ABAQUS/CAE. However, only the finite element mesh will have to be regenerated in ABAQUS.

Identifying the optimal mesh is necessary to provide better results due to the sensitivity of the finite element models to the size and number of elements. Because of the complexity of the geometrical lattice shapes, the model can only accept the tetrahedron mesh (element type C3D4) with free technique as shown in Fig. 3. Subsequently, the optimum numbers of the elements need to be identified using the mesh type C3D4. To determine that number, the model was required to run with the default number of elements to observe the maximum displacement and force. For this reason, the model had been rerun several times with different numbers of elements until the convergence was reached as shown in Fig. 4(a) and (b). It is observed that the reaction force increases and the displacement decreases with increasing number of elements. The lattice models of poor mesh density created with larger size elements show lower stiffness and more flexibility due to not filling the complicated regions of the lattice geometry accurately, thereby exhibiting lower reaction forces, while the reverse is true. In other words, the fine mesh density associated with higher number of smaller elements can cover the most complicated areas of the lattice geometry, by this way providing stiffer mechanical behavior and higher reaction forces. These figures show the number of elements corresponding to both the yielding force and the maximum displacement for BCC configuration. In this regard, the minimum number of the elements at which the convergence occurred was noticed about 550,000. Next, identifying the mass scaling was important to minimize the computational time. According to Simulia (Ref 21), the mass scaling is a factor to control the incrementing of the time based on the density of the specific elements. Similarly, the mass scaling was identified by rerunning the model and observing the maximum displacement until the convergence was satisfied, as shown in Table 1.

3.2 Development of Impact Model

The ASTM standard D7136 low-velocity impact machine was used for the experimental tests (Ref 1). Based on the capacity of the impact testing machine, the maximum drop height was considered as 621.5 mm. As the impactor released from a height of 621.1 mm, the velocity of the impactor right before contact with the sample was calculated to be 3492 mm/s using Eq 1 (Ref 18). This calculated velocity is termed here as 'initial velocity' in the manuscript.

$$v = \sqrt{2gh} \qquad \text{(Eq 1)}$$
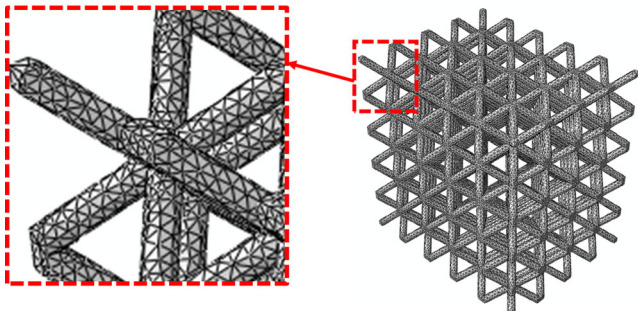
where g is the gravitational acceleration with a value of 9805 mm/s^2, and h is the drop height of 621.5 mm.

The mass of the impactor was 2436 g, and hence, the kinetic energy (KE) of the impactor as it hits the specimen can be calculated using Eq 2.
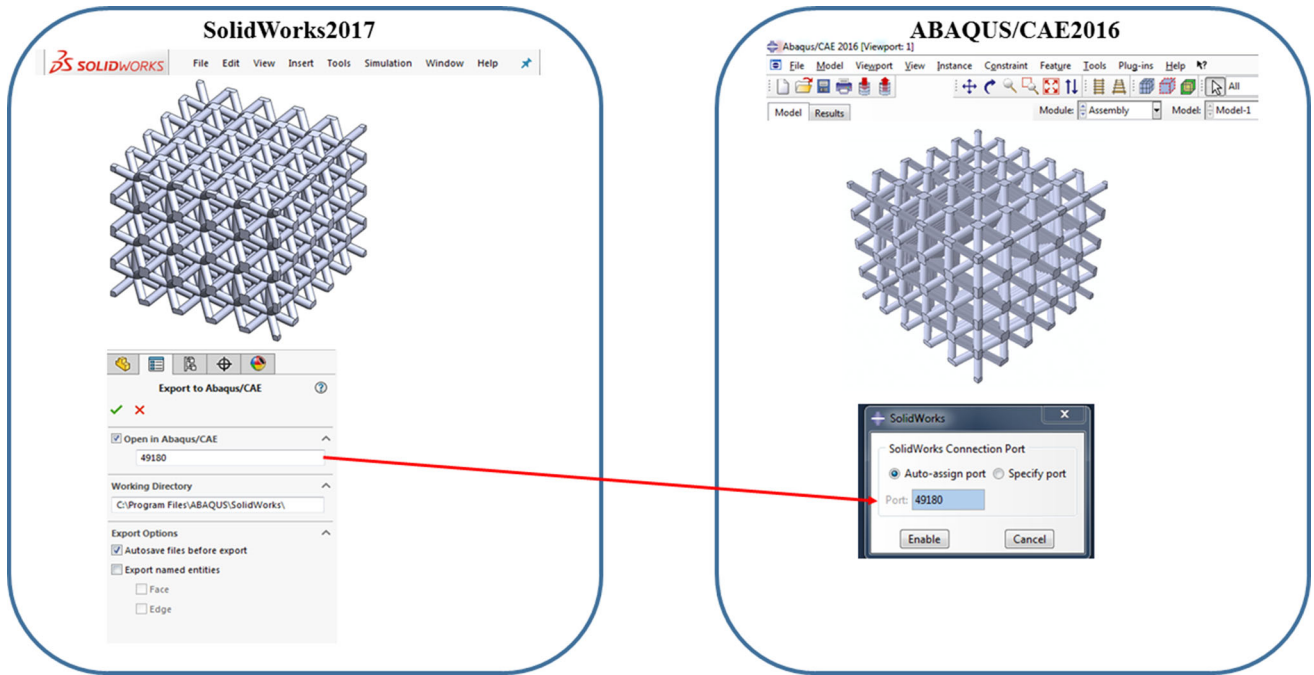
**Fig. 2** Using ABAQUS Associative Interface tool to export the Lattice from SolidWorks to ABAQUS/CAE

Fig. 3 BCC lattice configuration meshed with tetrahedron element type (C3D4)

$$KE = \frac{1}{2}mv^2 \qquad\qquad (\text{Eq 2})$$

where m is the mass of the impactor of 2436 g, and v is the impactor velocity at the moment of hitting the sample and equal to 3492 mm/s. Here, the energy loss due to the friction between the impactor assemblies was considered negligible (Ref 1).

Due to the nature of loading and boundary conditions, the FEA was performed only on symmetric quarter models. The overall dimension of each quarter model was 25 mm × 25 mm × 20 mm, and the symmetric boundary conditions were applied in the X and Y directions as shown in Fig. 5(a) and (b). Since the quarter model was used for the impactor as well, the quarter of the impactor mass was considered in this case, which was 609 g. However, the impactor velocity and acceleration
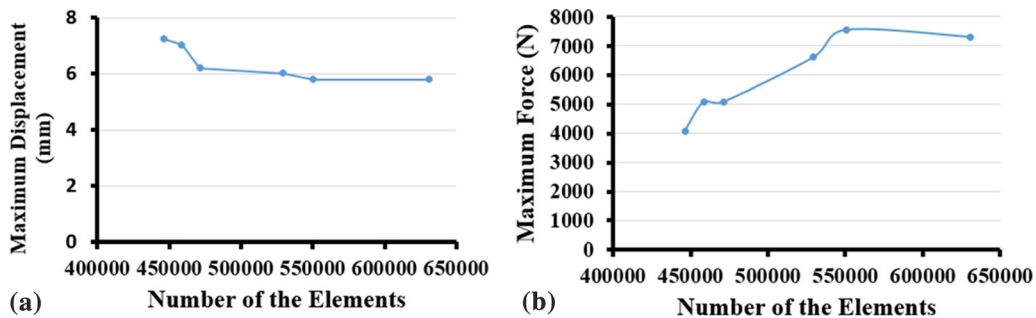
Fig. 4 The convergence analyses relative to the number of the elements based on the maximum (a) displacement and (b) force

Table 1 The convergence analyses of the maximum displacement due to the time scaling value

| Time scaling value	Maximum displacement, mm	Time scaling value	Maximum displacement, mm
0.01	2.560	1E-6	7.221
0.001	5.02	1E-7	7.786
0.0001	6.112	1E-8	7.795
1E-5	6.850	1E-9	7.801
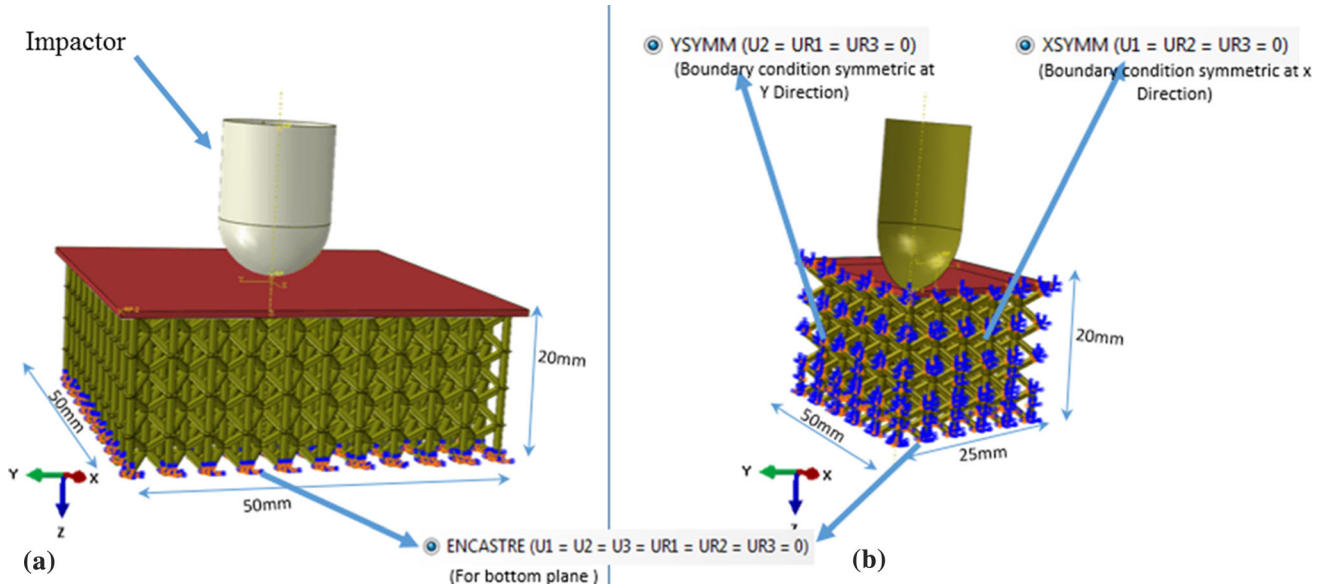
Fig. 5 Boundary conditions for the modeling of (a) entire model and (b) symmetric quarter model

were considered the same. The load in this case was applied as a sudden initial velocity of 3493 mm/s starting from the moment the impactor hits the top surface. As the model is run, the software calculates the impactor displacement at different time steps as the impactor travels in the thickness direction of the sandwich structure. The impactor displacement as well as the deformation of the sandwich structure depends on the mechanical properties of the skin and the lattice core configuration.

All the material properties have to be defined precisely and accurately before logging them in the ABAQUS/CAE software (Ref 2, 3). The sandwich structure specimens were built with ABS lattice cores and skin on the top made from Kevlar 49 sheet. The ABS properties were identified experimentally by printing ASTM D-638 standard (Ref 30) samples in our previous study (Ref 21). From the stress–strain curve of the tested samples, Young's modulus of the 3D-printed ABS material was measured as 861.6 MPa. The other required properties of printed ABS such as the Poisson's ratio and the density were considered to be 0.35 and 7.92E-4 g/mm³, respectively (Ref 28). The plasticity range of the printed material is shown in Fig 6, starting with 25.3 MPa yield strength. Similarly, the mechanical properties of the Kevlar 49 were measured experimentally and extracted from the stress–strain plot. The density was found to be 1.44e-4 g/mm³, Young modulus was considered to be 86,000 MPa and Poisson's ratio to be 0.36 (Ref 4). The fracture criteria were based on the plastic deformation and failure using ductile and shear damage criteria (Ref 3). Both the ductile and shear damages were
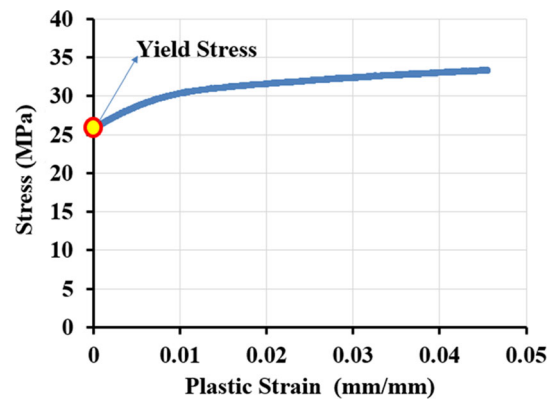
Fig. 6 Stress–strain behavior of the bulk ABS in the plasticity region used in the FEA model

identified based on the fracture strain, stress triaxiality η, shear stress ratio θ_s, and strain rates $\dot{\varepsilon}$ (Ref 1). According to Ref 1, the tensile tests were used to identify the fracture strains and strain rates, whereas the stress triaxiality η was computed from Eq 3 and the shear ratio θ_s was computed from Eq 5.

$$\eta = -\frac{p}{q} = \frac{-\frac{1}{3}(\sigma_1 + \sigma_2 + \sigma_3)}{q} \qquad \text{(Eq 3)}$$

where p is hydrostatic pressure and q is the von Mises stress computed from Eq 4.

$$q = \sqrt{\frac{(\sigma_1 - \sigma_2)^2 + (\sigma_2 - \sigma_3)^2 + (\sigma_3 - \sigma_1)^2}{2}} \qquad \text{(Eq 4)}$$

where σ_1, σ_2, σ_3 are the principal stresses. The shear stress ratio θ_s is calculated from Eq 5

$$\theta_s = \frac{(q + K_s p)}{\tau_{\max}} \qquad \text{(Eq 5)}$$

where $\tau_{\max}$ is the maximum shear stress and can be calculated using Eq 6, and K_s is the material parameter.

$$\tau_{\max} = \frac{\sigma_1 - \sigma_3}{2} \qquad \text{(Eq 6)}$$

3.3 Discussion

After running the models, the plots of acceleration–time, velocity–time, and displacement–time were extracted from the ABAQUS FEA software on which all the results have been discussed. The simulation run time was 2 h for each model due to complicated formulation of explicit dynamics and higher number of the elements. In addition, the validation of the FEA models and the comparison of the results with the experimental works have been presented. The results of the current investigation will be discussed and utilized in the following paragraphs.

The FEA models of the impact test revealed that the peak loads and maximum displacements are in a good agreement with the experimental observations. For example, according to the plots of BCC configuration shown in Fig. 7, the experimental peak forces were (2200–2700) N for three samples (Ref 1) and the finite element peak force is 2510.2 N. Thus, the

variance between the average of the experimental work and the finite element is 4.24%. Also, the computational maximum displacement of the impactor is 8.9 mm, while the maximum experimental displacements were observed to be 8.1–9.0 mm (Ref 1), with the variance of about 1.14%, whereas based on the velocity plots, the experiment velocities of the impactor upon separation were seen to be 280–1250 mm/s (Ref 1) and the same obtained from FEA is 1010 mm/s as shown in Fig. 7(b). From the velocity plot, the absorbed energy was calculated based on the difference in the kinetic energies before and after hitting the impactor with the sandwich lattice structure. The average of the experimental of the absorbed energy of the BCC was 13.8 J, and the finite element was 12.7 J with the variance of 7.97%. In the same manner, the finite element models for all other configurations such as BCCA, BCCG, and BCCV have provided reasonable values along with giving more details for all the impact simulations. Both the experimental and finite element models have shown good agreement and correlations. Comparisons of key impact characteristics obtained from FEA and published experimental results are summarized in Table 2 for all four configurations. The summary results shown in Table 2 are obtained from Fig. 7, 8, 9, and 10.

From the FEA simulation, the in situ progressive damage can be easily studied and analyzed by capturing the indentation depth. The lattice layers are referred to as I for the first layer until IV for the fourth as shown in Fig. 11, which shows the displacement contour plots for all four configurations. Figure 12(a) through (d) shows the load-displacement plot from FEA. The two positions of the impactor were identified as shown in Fig. 12, position (i) and (ii). The position (i) is used to express the maximum distance that the impactor traveled in the downward direction from the location of first contact with Kevlar sheet. At this position, the impactor velocity is zero and
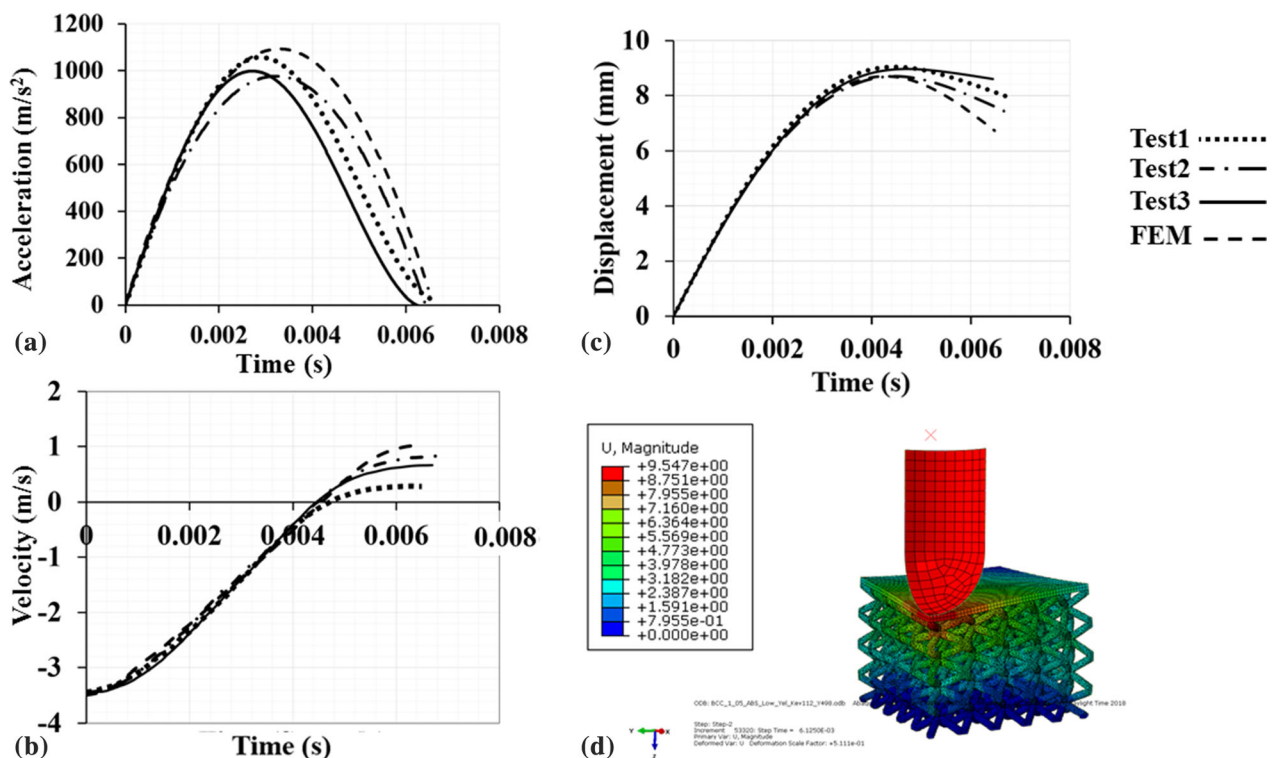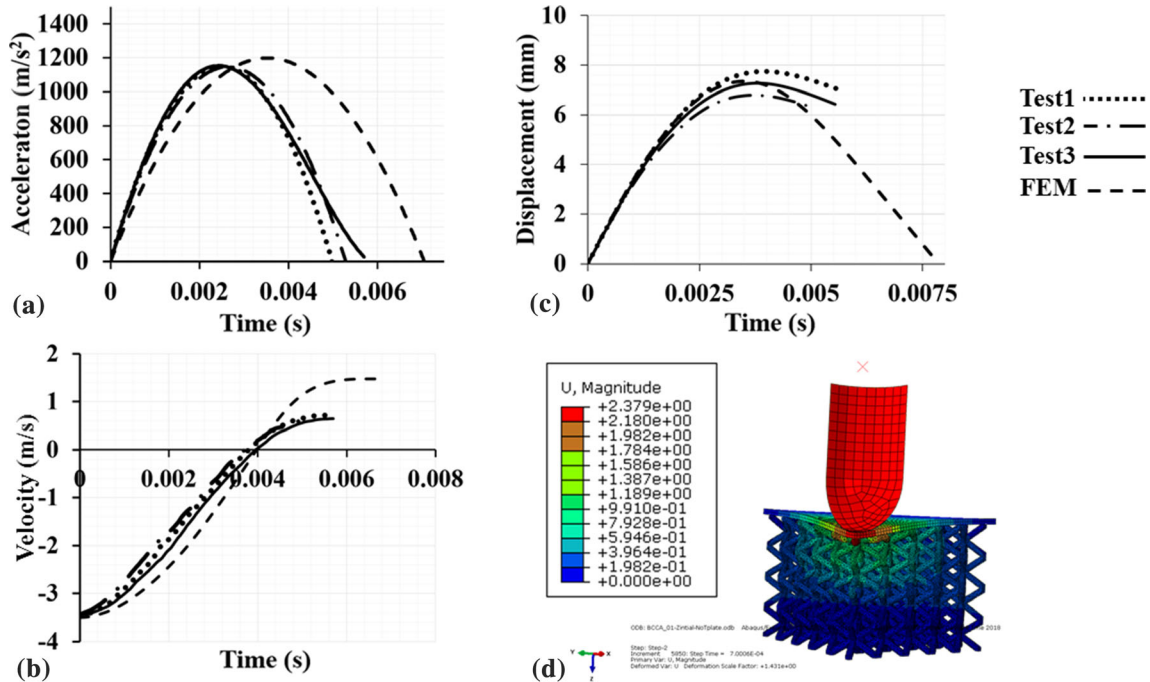

Fig. 7 BCC impact, FEA model results. Plots of (a) acceleration–time, (b) velocity–time, (c) displacement–time, and (d) displacement contour

Table 2 Summary of key low-velocity impact characteristics of all configurations

Configuration		BCC	BCCA	BCCG	BCCV
Peak load (N)	Exp. Avg.	2408.10	2766.66	2775.01	3627.50
	FEA	2510.20	2944.20	2951.10	3912.33
	The coefficient of variance (%)	−4.24%	−6.42%	−6.35%	−7.85%
Max displacement (mm)	Exp. Avg.	8.8	7.4	7.4	6.0
	FEA	8.9	7.4	8.3	6.1
	The coefficient of variance (%)	1.14%	0.00%	12.16%	1.67%
Absorbed energy (J)	Exp. Avg.	13.77	13.57	13.55	12.94
	FEA	12.64	11.51	11.51	10.41
	The coefficient of variance (%)	−7.97%	−14.07%	−14.74%	−16.28%

Fig. 8 BCCA impact, FEA model results. Plots of (a) acceleration-time, (b) velocity-time, (c) displacement-time, and (d) displacement contour

changes its direction. The position (ii) is when the impactor separates from Kevlar sheet after the elastic recovery of the Kevlar sheet and the whole sandwich structure. At this point, the force drops to a zero and indicates the depth of the indentation mark on the Kevlar surface. For the BCC configuration, the maximum indentation depth indicated by position (i) was 8.99 mm as shown in Fig. 12(a). However, the damage due to the impact goes beyond 8.99 mm and a total damage depth of approximately 10 mm consisting of the top two layers of the lattice core (III and IV) is observed. The damage depth observed from FEA is similar to that observed from X-ray images of the post-impacted BCC samples reported in reference (Ref 1). It is observed from the FEA image (Fig. 11a) that layer IV is totally crushed, while layer III is partially damaged where several struts are seen to be failed. Besides, the depth associated with position (ii) from Fig. 11(a) is observed to be 6 mm after the elastic recovery. Thus, the BCC configuration has approximately 2.99 mm elastic recovery as the impactor travels in the upward direction and separates from the Kevlar sheet. For BCCA configuration, the maximum indentation depth allocated

at position (i) was captured as 7.44 mm as shown in Fig. 11(b). In this regard, the associated damage failure was observed to grow through the layers IV, III, and partially in II. In other words, the impact influence moves deep inside the lattice core for over 12.5 mm corresponding to the total height of two and a half layers even though the maximum indentation depth is just 7.44 mm. Specifically, the layers IV and III are totally collapsed and only the lower struts of layer II are almost left without any damage as noticed in Fig. 11(b). To clarify that, the vertical struts which are located between the layers III and IV have transferred the impact force directly to layer II and, consequently, the layer II has partially collapsed. Also, the indentation depth of location (ii) from Fig. 12(b) is estimated to be 6.23 mm such that the BCCA sandwich structure can have a little amount of elastic recovery with a value of 1.21 mm. This means the layers III and IV will not recover after the fatal failure. For the BCCG configuration, the layers III and IV are observed to be collapsed as shown in Fig. 11(c). The maximum indentation depth at location (i) is determined as 8.3 mm from Fig. 12(c), and the impact damage through the lattice core can
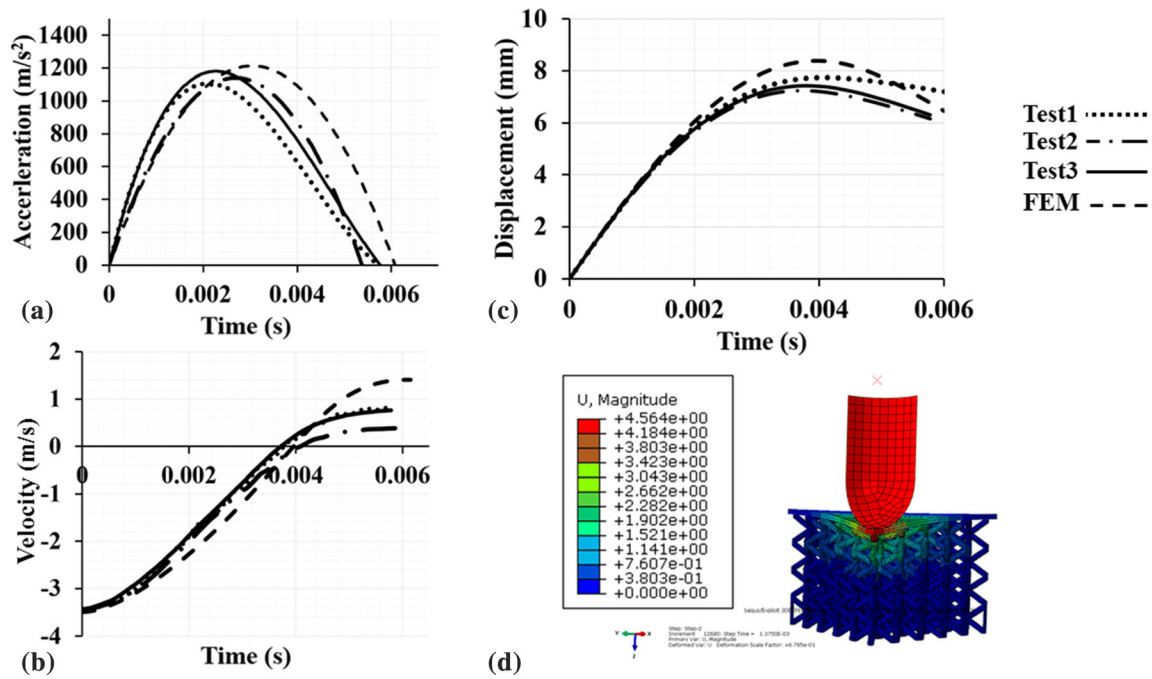
Fig. 9 BCCG impact, FEA model results. Plots of (a) acceleration-time, (b) velocity-time, (c) displacement-time, and (d) displacement contour
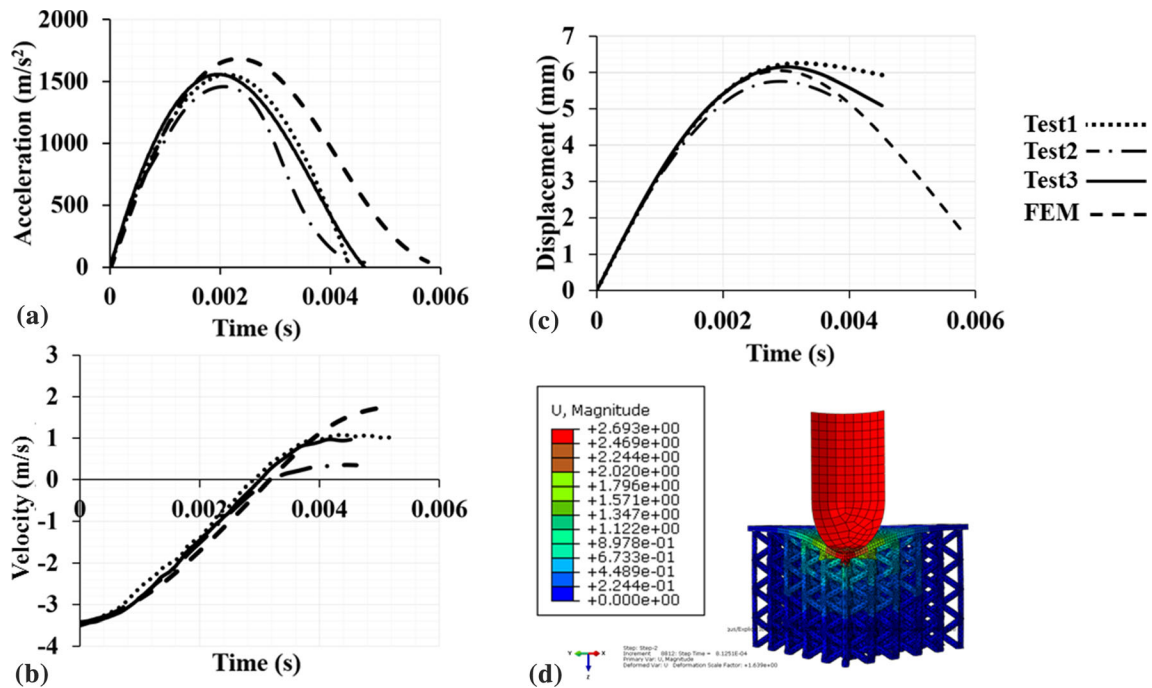

Fig. 10 BCCV impact, FEA model results. Plots of (a) acceleration-time (b) velocity-time (c) displacement-time, and (d) displacement contour

reach more than 12.5 mm corresponding to the layers IV, III, and II. In this regard, the layers IV and III are totally crushed and the layer II has a partial rubble in the upper pillars. In addition, the indentation depth after elastic recovery (location (ii)) is about 6.4 mm so that BCCG configuration can have an elastic recovery of 1.89 mm. For the last configuration (BCCV), the maximum indentation depth at position (ii) is 6.1 mm as it can be seen in Fig. 12(d). This in turn corresponds

to 10 mm damage failure through lattice core within the layers IV and III, which are totally collapsed as shown in Fig. 11(d). According to Fig. 12(d), the indentation depth of position (ii) after elastic recovery is found to be 1.98 mm. For this reason, BCCV sandwich structure offers large elastic recovery of 4.13 mm. This is due to the higher stiffness of the BCCV configuration owing to the addition of vertical struts distributed at each node of the entire lattice core structure.
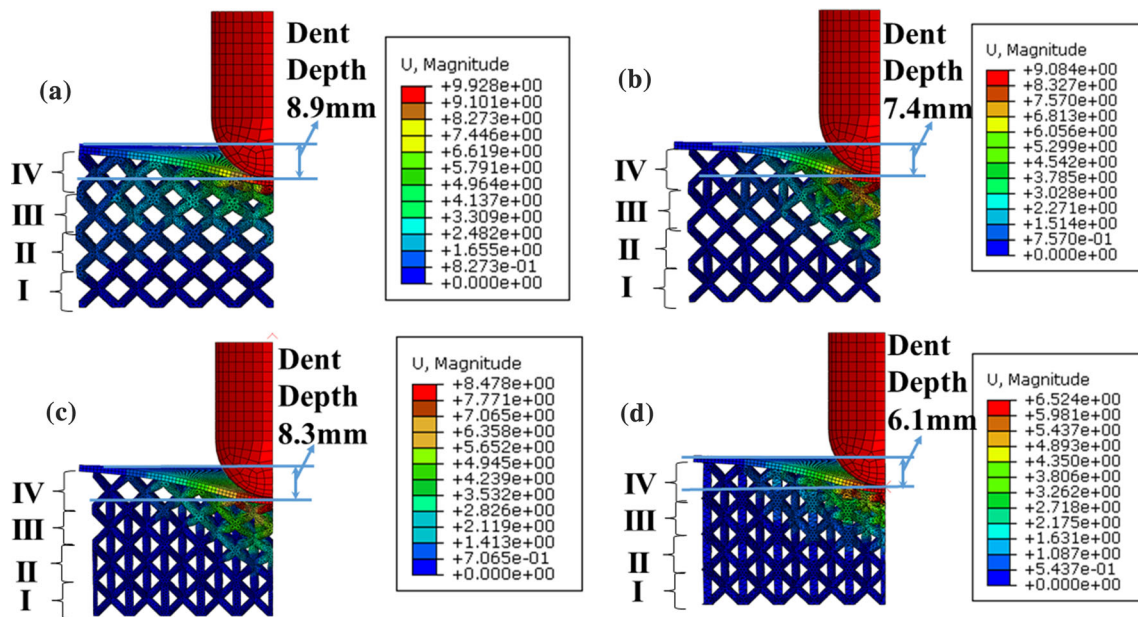
Fig. 11 Displacement contour plots showing maximum depth indentation for (a) BCC, (b) BCCA (c) BCCG, and (d) BCCV configurations

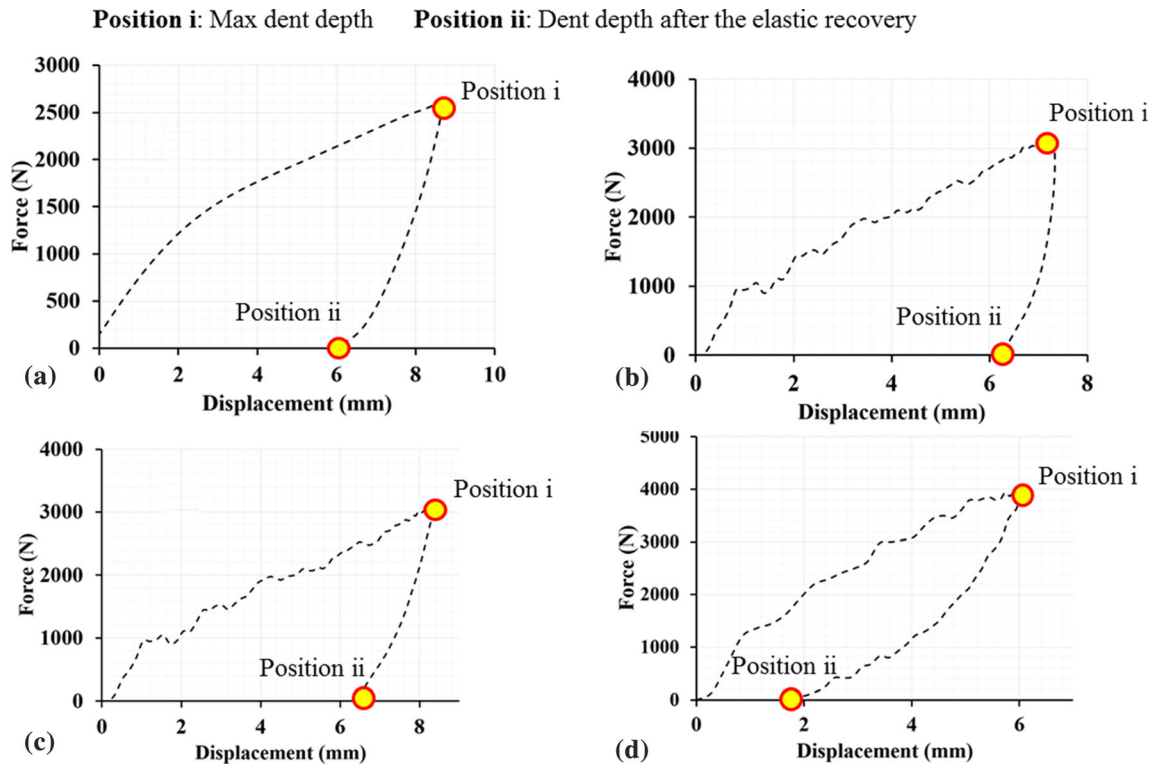**Position i**: Max dent depth   **Position ii**: Dent depth after the elastic recovery

Fig. 12 Force-displacement plots based on FEMs for (a) BCC, (b) BCCA, (c) BCCG, and (d) BCCV configurations

4. Conclusions

In this research, the finite element models have been developed for impact test ASTM D7136 of sandwich structures made from ABS lattice cores. Due to the complexity of the lattice geometry, SolidWorks/ABAQUS associative interface tool has been used to create the lattice structure models. The tool can offer direct connection between SolidWorks and ABAQUS, thereby providing an efficient technique to edit,

change, or manipulate the lattice structural parameters. The model results have been validated and evaluated based on the experimental work from previous studies. Significantly, good agreement between the FEA results and the experimental findings has been achieved in the current investigation and the key conclusions of the current research can be summarized as follows.

- The developed finite element models have shown good capabilities in capturing the dynamic impact behavior of

various lattice configurations, starting with the basic feature of lattice (BCC), then moving to a modified lattice pattern (BCCA), and ending with complicated lattice generations (BCCG and BCCV). This is in turn not only proving the efficiency of the adopted computational models but also making them a more general purpose to predict the impact deformation behavior for further lattice configurations.

- The dynamic models developed in the current research can easily capture the in situ impact deformation and failure mechanisms from the moment at which the impactor hits the sandwich surface where the force and displacement equal zero till reaching the maximum indentation depth (position I) accompanied with the highest values of force and displacement. Besides, these models have revealed the recovery deformation path from position I to position II after the impactor traveled back and moved away from the sandwich surface. This path plays a major role in the analyses of lattice impact resistance, and it is very hard to be captured experimentally.

- Detailed information and sufficient data have been provided in a competitive time through developing these models, such as the reaction force, indentation depth, velocity, acceleration, and absorbed energy as well as visualization or animation for the entire impact behavior which could provide a better insight and understanding for the researchers than the experimental work which in most cases is costly and require expensive tools to provide similar information and data.Based on the aforementioned conclusions, the dynamic computational finite element models developed in the current research could have significant contribution in saving human time and effort as well as reducing the expenses associated with the experimental work.

References

1. M. Al Rifaie, A. Mian, P. Katiyar, P. Majumdar and R. Srinivasan, Drop-Weight Impact Behavior of Three-Dimensional Printed Polymer Lattice Structures with Spatially Distributed Vertical Struts, *J. Dyn. Behav. Mater.*, 2019, **5**(4), p 387–395

2. J.J. Andrew, J. Schneider, J. Ubaid, R. Velmurugan, N.K. Gupta and S. Kumar, Energy Absorption Characteristics of Additively Manufactured Plate-Lattices Under Low- Velocity Impact Loading, *Int. J. Impact Eng.*, 2020, **149**, p 103768

3. S. Guessasma, S. Belhabib, D. Bassir, H. Nouri and S. Gomes, On the Mechanical Behaviour of Biosourced Cellular Polymer Manufactured using Fused Deposition Modelling, *Polymers*, 2020, **12**(11), p 1–15

4. J.A. Harris and G.J. McShane, Impact Response of Metallic Stacked Origami Cellular Materials, *Int. J. Impact Eng.*, 2020, **147**, p 103730

5. C. Tang, J. Liu, Y. Yang, Y. Liu, S. Jiang and W. Hao, Effect of Process Parameters on Mechanical Properties of 3D-Printed PLA Lattice Structures, *JCOMC*, 2020, **3**, p 100076

6. C. Pan, Y. Han and J. Lu, Design and Optimization of Lattice Structures: A Review, *Appl. Sci.*, 2020, **10**(18), p 6374

7. S.K. Moon, Y.E. Tan, J. Hwang, J. Hwang and Y.J. Yoon, Application of 3D Printing Technology For Designing Light-Weight Unmanned Aerial Vehicle Wing Structures, *Int. J. Precis. Eng. Manuf-Green Tech.*, 2014, **1**(3), p 223–228

8. L. Magerramova, M. Volkov, A. Afonin, M. Svinareva, D. Kalinin, Application of light lattice structures for gas turbine engine fan blades. In, *31st Congress of the International Council of the Aeronautical Sciences, ICAS 2018*, pp. 1–10, 2018. https://www.icas.org/ICAS_A RCHIVE/ICAS2018/data/papers/ICAS2018_0173_paper.pdf. Accessed 15 May 2021

9. A.S. Alagoz and V. Hasirci, 3D Printing of Polymeric Tissue Engineering Scaffolds Using Open-Source Fused Deposition Modeling, *Emerg. Mater.*, 2020, **3**(4), p 429–439

10. A. Forget, T. Derme, D. Mitterberger, M. Heiny, C. Sweeney, L. Mudili, T.R. Dargaville and V.P. Shastri, Architecture-Inspired Paradigm for 3D Bioprinting of Vessel-like Structures Using Extrudable Carboxylated Agarose Hydrogels, *Emerg. Mater.*, 2019, **2**(2), p 233–243

11. M.K. Deshmukh, K. Chidambaram, M.B. Ahamed, K.K. Sadasivuni, D. Ponnamma, M.A.A. AlMaadeed, R.R. Deshmukh and S.K. Pasha, Polyvinyl Alcohol (PVA)/Polystyrene Sulfonic Acid (PSSA)/Carbon Black Nanocomposite for Flexible Energy Storage Device Applications, *J. Mater. Sci. Mater.*, 2017, **28**(8), p 6099–6111

12. T. Dayakar, K.V. Rao, K. Bikshalu, V. Malapati and K.K. Sadasivuni, Non-Enzymatic Sensing of Glucose Using Screen-Printed Electrode Modified with Novel Synthesized CeO2@CuO Core Shell Nanostructure, *Biosens. Bioelectron.*, 2018, **111**, p 166–173

13. J. Gounder Thangamani, K. Deshmukh, K.K. Sadasivuni, D. Ponnamma, S. Goutham, K. Venkateswara Rao, K. Chidambaram, M. Basheer Ahamed, A. Nirmala Grace, M. Faisal and S.K. Khadheer Pasha, White Graphene Reinforced Polypyrrole and Poly(Vinyl Alcohol) Blend Nanocomposites as Chemiresistive Sensors for Room Temperature Detection of Liquid Petroleum Gases, *MCA*, 2017, **184**(10), p 3977–3987

14. A. Nagaraj, K.K. Sadasivuni and M. Rajan, Investigation of Lanthanum Impregnated Cellulose, Derived from Biomass, as an Adsorbent for the Removal of Fluoride from Drinking Water, *Carbohydr. Polym.*, 2017, **176**, p 402–410

15. Y. Shen, W. Cantwell, R. Mines and R. Li, Low-Velocity Impact Performance of Lattice Structure Core Based Sandwich Panel, *J. Compos. Mater.*, 2014, **48**, p 3153–3167

16. S.A. Galehdari, M. Kadkhodayan and S. Hadidi-Moud, Low Velocity Impact and Quasi-Static In-plane Loading on a Graded Honeycomb Structure; Experimental, Analytical and Numerical Study, *Aerosp. Sci. Technol.*, 2015, **47**, p 425–433

17. J.A. Harris, R.E. Winter and G.J. McShane, Impact Response of Additively Manufactured Metallic Hybrid Lattice Materials, *Int. J. Impact Eng.*, 2017, **104**, p 177–191

18. B. Castanié, C. Bouvet, Y. Aminanda, J.J. Barrau and P. Thevenet, Modelling of Low-Energy/Low-Velocity Impact on Nomex Honeycomb Sandwich Structures with Metallic Skins, *Int. J. Impact Eng.*, 2008, **35**(7), p 620–634

19. L.B. Hussain and I.A. Hakim, Recycling and Formulation of Aluminum Scrap Via Mass Balance Die Casting and Forming, *Mater. Manuf. Process.*, 2007, **22**(7), p 916–921

20. H. Abdulhadi and A. Mian, Effect of Strut Length and Orientation on Elastic Mechanical Response of Modified Body-Centered Cubic Lattice Structures, *Proc. Inst. Mech. Eng. L -JMDA*, 2019, **223**(11), p 2219–2233

21. A. Fadeel, A. Mian, M. Al Refaie and R. Srinivasan, Effect of Vertical Strut Arrangements on Compression Characteristics of 3D Printed Polymer Lattice Structures: Experimental and Computational Study, *J. Mater. Eng. Perform.*, 2018, **1**, p 1–8

22. R. Mines, S. Tsopanos, E. Shen, S. McKown, W. Cantwell, W. Brooks and C. Sutcliffe, *On the Performance of Micro Lattice Structures as Core Materials in Sandwich Panels Subject to Low Velocity Impact*, Department of Engineering The Quadrangle, University of Liverpool, Liverpool, UK, 2009

23. J. Wang and B.V. Sankar, Fracture Toughness of Cellular Materials Using Finite Element Based Micromechanics, *J. Chem. Inf. Model.*, 2013, **53**(9), p 1689–1699

24. K.R. Jagtap, S.Y. Ghorpade and A.L. Singh, Finite Element Simulation of Low Velocity Impact Damage in Composite Laminates, *Mater. Today Proc.*, 2017, **4**(2), p 2464–2469

25. Y. Bao and T. Wierzbicki, On Fracture Locus in the Equivalent Strain and Stress Triaxiality Space, *Int. J. Mech. Sci.*, 2004, **46**(1), p 81–98

26. X. Wang and J. Shi, Validation of Johnson-Cook Plasticity and Damage Model Using Impact Experiment, *Int. J. Impact Eng.*, 2013, **60**, p 67–75

27. Abaqus CAE User's Guide, DS Simulia Abaqus 2016. http://abaqus. software.polimi.it/v2016/books/usi/default.htm. Accessed 15 May 2021

28. H.S. Abdulhadi, Designing New Generations of BCC Lattice Structures and Developing Scaling Laws to Predict Compressive Mechanical Characteristics and Geometrical Parameters. *Ph.D. dissertation, Wright State University, Dayton, Ohio,* pp. 171, 2020. http://rave.ohiolink.edu/etdc/view?acc_num=wright1610335306482598. Accessed 15 May 2021

29. A.J. Turner, M. Al Rifaie, A. Mian and R. Srinivasan, Low-Velocity Impact Behavior of Sandwich Structures with Additively Manufactured Polymer Lattice Cores, *J. Mater. Eng. Perform.*, 2018, **27**(5), p 2505–2512

30. J.J. Laureto and J.M. Pearce, Anisotropic Mechanical Property Variance Between ASTM D638–14 Type i and Type iv Fused Filament Fabricated Specimens, *Poly. Test.*, 2018, **68**, p 294–301